Chemical Engineering Journal 359 (2019) 924–932

Contents lists available at ScienceDirect

Chemical Engineering Journal

journal homepage: www.elsevier.com/locate/cej

A new photocatalyst based on $Co(CO_3)_{0.5}(OH)\cdot 0.11H_2O/Bi_2WO_6$ nanocomposites for high-efficiency cocatalyst-free O_2 evolution

Bin He[a,1], Huanhuan Liu[a,1], Zheng Lin[b], Lei Yan[a], Jiqiang Ning[c], Yijun Zhong[a], Changcheng Zheng[d], Ziyang Zhang[c], Yong Hu[a,*]

[a] Key Laboratory of the Ministry of Education for Advanced Catalysis Materials, Department of Chemistry, Zhejiang Normal University, Jinhua 321004, China
[b] School of Materials Science and Engineering, Beihang University, Beijing 100191, China
[c] Vacuum Interconnected Nanotech Workstation, Suzhou Institute of Nano-Tech and Nano-Bionics, Chinese Academy of Sciences, Suzhou 215123, China
[d] Mathematics and Physics Centre, Department of Mathematical Sciences, Xi'an Jiaotong-Liverpool University, Suzhou 215123, China

HIGHLIGHTS

- A novel and high-efficiency photocatalyst based on CCO/BWO nanocomposite was firstly synthesized.
- CCO/BWO nanocomposite was prepared via a facile hydrothermal method.
- CCO/BWO nanocomposite exhibits extraordinarily high photoactivity towards O_2 evolution without additional of any cocatalyst.

GRAPHICAL ABSTRACT

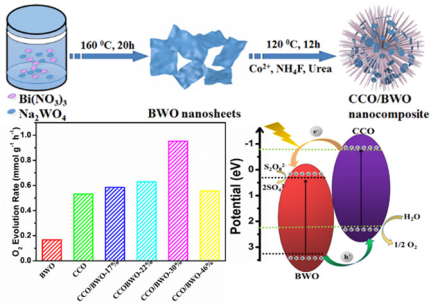

ARTICLE INFO

Keywords:
$Co(CO_3)_{0.5}(OH)\cdot 0.11H_2O$
Bi_2WO_6
Nanocomposite
Photocatalytic O_2 evolution
Cocatalyst-free

ABSTRACT

The practical application of photocatalytic water splitting is essentially limited by the slow kinetic nature of the water oxidation process. Therefore, it is highly desirable but challenging to explore a low-cost and high-efficiency water oxidation catalyst for the aim of commercialization and industrialization. We herein report the first-time synthesis of a novel and high-efficiency visible-light-driven photocatalyst composed of flower-like Co $(CO_3)_{0.5}(OH)\cdot 0.11H_2O$ (CCO) nanowires and Bi_2WO_6 (BWO) nanosheets, *i.e.* CCO/BWO nanocomposite, via a facile hydrothermal method. Without utilizing any additional cocatalyst, the composite of CCO/BWO in 30% weight ratio exhibits extraordinarily high photoactivity and photostability towards O_2 evolution, achieving an average O_2 generation rate of 953 $\mu mol\ h^{-1}\ g^{-1}$ under visible-light irradiation ($\lambda > 420$ nm).

1. Introduction

With the industrial development and economic growth of human society, the dramatically increasing demand for energy couples with the environmental deterioration [1–3]. Among various green earth and renewable energy projects, photocatalytic water splitting has been regarded as a cost-effective and green technology utilizing solar energy [4–6]. Owing to the slow kinetics of four-electron transfer and the high activation energy barrier for oxygen-oxygen bond, water oxidation is the rate-determining step in photocatalytic water splitting process, and it is very challenging to find high-efficiency water oxidation catalysts [7,8]. Especially, in terms of commercialization and industrialization,

* Corresponding author.
E-mail addresses: yonghu@zjnu.edu.cn, yonghuzjnu@163.com (Y. Hu).
[1] These authors contributed equally to this work.

https://doi.org/10.1016/j.cej.2018.11.094
Received 4 September 2018; Received in revised form 25 October 2018; Accepted 12 November 2018
Available online 13 November 2018
1385-8947/

high activity and low-cost photocatalysts for water splitting are highly desirable.

Recently, a series of cobalt-based semiconductors have been widely investigated as photocatalysts and electrocatalysts for efficient water oxidation, including cobalt oxide [9,10], cobalt hydroxide [11,12], chalcogenide [13], phosphide [14,15] nitride [16], and so on. Till now, cobalt carbonate hydroxide hydrate ($Co(CO_3)_{0.5}OH{\cdot}0.11H_2O$, CCO) has been recognized as a novel electrochemical material due to its superior performance, eco-friendly feature and low price [17]. As the anion (CO_3^{2-}) is inserted in the interlayer spacing of crystal lattice rather than at hydroxyl ion (OH^-) position in CCO, it possesses ideal ionic conductivity by building internal metallic bond, resulting in forming efficient electronic transmission paths to increase the electronic conductivity [18]. Moreover, the presence of CO_3^{2-} and OH^- anions in the CCO offers high hydrophilicity, which is desirable aspect for the rapid diffusion of electron. Therefore, CCO has also demonstrated outstanding electrochemical performances [19–21], but to the best of our knowledge, has not been reported about applications in photocatalytic water oxidation. On the other side, as one of the important Aurivillius oxides, Bi_2WO_6 (BWO), with a narrow band gap of about 2.8 eV, has been demonstrated to be a promising visible-light-driven photocatalyst for oxygen (O_2) evolution [22–24]. However, due to the low efficiency of light absorption and quick recombination of the photo-generated charge carriers, bare BWO always exhibits relatively poor photocatalytic performances [22]. To overcome these drawbacks, the strategy of coupling BWO with other semiconductors has been proposed to achieve the matching of energy band structures which is expected to break through the intrinsic limitations of single compound and improve the separation of photo-generated electron-hole pairs [25]. A series of BWO-based composite photocatalysts such as BWO/WO_3 [26], BWO/$BiVO_4$ [24], C_3N_4/BWO [27], $BiPO_4$/BWO [28] and AgBr/Ag//BWO [29], have been reported with enhanced photocatalytic activity in comparison with bare BWO.

In photocatalytic water splitting, some cocatalysts, noble metals or metal oxides are usually used to facilitate either the reduction or the oxidation of water [30,31]. Therefore, it is a challenge to develop completely cocatalyst-free photocatalysts for water oxidation. In this work, a novel high-efficiency visible-light-driven photocatalyst based on flower-like CCO nanowires and BWO nanosheets (CCO/BWO nanocomposite), has been prepared for the first time via a facile hydrothermal reaction occurring at 120 °C for 12 h, with only Co$(NO_3)_2{\cdot}6H_2O$, NH_4F, urea and different amounts of BWO nanosheets as the starting materials and without using any additional surfactant. Among all the obtained products, the composite of CCO/BWO in 30% weight ratio exhibits the highest photocatalytic activity for water oxidation under the visible-light irradiation with no cocatalyst. The dramatically enhanced photocatalytic activity can be attributed to the appropriate band alignment which facilitates the separation of photo-generated electron-hole pairs and improves the interfacial charge transfer efficiency. The band structure of the CCO/BWO composite system is characterized with UV–Vis diffuse reflectance spectroscopy (DRS) and Mott-Schottky plots. And photoluminescence (PL), photocurrent and electrochemical impedance spectroscopies (EIS) were employed to explore the charge separation and interfacial transfer behaviors. The governing mechanism underlying the enhanced photocatalytic activity of CCO/BWO photocatalyst will be discussed in details.

2. Experimental section

The reagents (all of analytical grade) employed in this work were purchased from Shanghai Chemical Reagent Factory, and utilized as received without further purification.

2.1. Material synthesis

Synthesis of BWO photocatalyst. In a typical synthetic procedure, 1 mmol $Na_2WO_4{\cdot}2H_2O$ and 2 mmol $Bi(NO_3)_3{\cdot}5H_2O$ were mixed in 100 mL of distilled water and then placed in an ultrasonic bath for 10 min to complete the precipitation reaction. The precipitate was collected and washed before being dissolved in 40 mL distilled water with ultrasonication for 30 min. After 30 min' further vigorous stirring, the mixture was sealed in a 50 mL Teflon-lined stainless-steel autoclave and placed in an oven at 160 °C for 20 h. The resulting product was collected by centrifugation, repeatedly washed with ethanol and distilled water before dried in an oven at 60 °C for 12 h.

Synthesis of CCO photocatalyst. In a typical synthetic procedure, 153 mg $Co(NO_3)_2{\cdot}6H_2O$, 26 mg NH_4F and 105 mg urea were dissolved in 35 mL of distilled water with the assistance of ultrasonication for 30 min. The mixture was sealed in a 50 mL Teflon-lined stainless-steel autoclave and then placed in an oven at 120 °C for 12 h. The product was collected by centrifugation, washed with ethanol and distilled water for at least three times, and finally dried in an oven at 60 °C for 12 h.

Synthesis of CCO/BWO hybrid photocatalyst. In a typical procedure, 153 mg $Co(NO_3){\cdot}6H_2O$, 26 mg NH_4F and 105 mg urea were dissolved in 35 mL distilled water, followed by the addition of 200, 150, 100, or 50 mg of BWO powder under ultrosonication for 30 min. After 30 min vigorous stirring, the mixture was sealed in a 50 mL Teflon-lined stainless-steel autoclave and heated at 120 °C for 12 h. Finally, the product was collected by centrifugation, repeatedly washed with ethanol and distilled water, and then dried in an oven at 60 °C for 12 h. The products with different CCO/BWO weight ratios (CCO to CCO/BWO) of 17, 22, 30 and 46 wt% are labeled as CCO/BWO-17%, CCO/BWO-22%, CCO/BWO-30% and CCO/BWO-46%, respectively. The schematic diagram for the synthesis of CCO/BWO nanocomposite is illuminated in Fig. 1 and all abbreviations in this manuscript are listed in Table S1.

2.2. Characterizations

The crystallinity and purity of the CCO/BWO samples were characterized by powder X-ray diffraction (XRD) measurements performed on a Philips PW 3040/60 X-ray diffractometer using the Cu Kα radiation. Scanning electron microscopy (SEM) characterization was carried out on a Hitachi S-4800 scanning electron micro-analyzer with an accelerating voltage of 15 kV. The as-prepared samples were also analyzed with the techniques of transmission electron microscopy (TEM) and high-resolution TEM (HRTEM) using a JEOL JEM-2100F microscope. The surface composition of the samples were performed by X-ray photoelectron spectroscopy (XPS), using an ESCALab MKII X-ray photoelectron spectrometer with Mg Kα X-ray as the excitation source. UV–vis DRS spectra were acquired over the spectral range of 200–800 nm in the absorption mode of a Thermo Nicolet Evolution 500 UV–vis spectrophotometer equipped with an integrating sphere attachment. Electron spin resonance (ESR) spectra were carried on a JEOL JES-FA200 ESR spectrometer at room temperature. 5,5-Dimethyl-1-pyrroline N-oxide (DMPO) was added to the solution as a spin trap to stabilize radicals. PL spectra were also measured using an excitation wavelength of 300 nm on a FLS 920 fluorescence spectrophotometer. Mott-Schottky measurements were performed at a frequency of 1 kHz

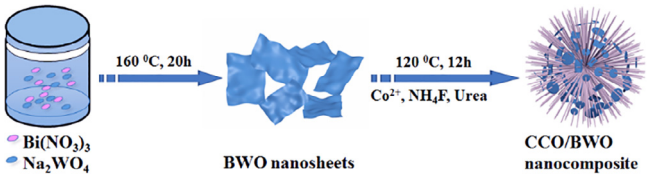

Fig. 1. Schematic diagram for the synthesis of CCO/BWO nanocomposite.

with the amplitude of 10 mV, with various potentials applied to a standard three-electrode cell on a Zennium E station (ZAHNER, Germany) which employs 0.5 M Na_2SO_4 as the electrolyte solution, a platinum wire as the counter electrode, and Hg/Hg^{2+} in saturated KCl as the reference electrode [32,33]. EIS measurements were also carried out in the three-electrode system on the Zennium E station with a $K_3[Fe(CN)_6]$ (5 mM) and KCl (1 M) aqueous solution, by applying an AC voltage of 10 mV with the frequency ranging from of 10 Hz to 100 kHz.

2.3. Photocatalytic O_2 evolution experiments

The photocatalytic O_2 evolution reactions were carried out in a closed reactor connecting to a water bath to maintain the reaction temperature at 25 ± 2 °C. The suspension was irradiated by a 300 W Xe lamp (MicroSolar 300, Perfect Light) equipped with an cut-on optical filter at 420 nm to block the light in the ultraviolet region. In a typical reaction, 20 mg photocatalyst was dispersed in 50 mL aqueous solution containing the sacrificial agents of 0.1 M NaOH and 0.02 M $Na_2S_2O_8$. Before photocatalytic experiments, the reaction vessel was purged with argon for at least 60 min to remove the dissolved air. The photocatalytic O_2 evolution reactions were conducted on a Labsolar-III AG system, with a Pyrex reaction vessel connected to an online gas chromatograph (Agilent Technologies GC-7890B, TCD, Ar carrier). The apparent quantum efficiency (QE) of the CCO/BWO-30.0% sample was defined by the Eq. (1) [33]:

$$QE[\%] = \frac{\text{the number of reacted electrons}}{\text{the number of incident photos}} \times 100\% = \frac{\text{the number of envolved } O_2 \text{ molecules} \times 4}{\text{the number of incident photos}} \times 100\% \quad (1)$$

2.4. ^{18}O isotope-labeling experiment

0.02 g of NaOH and 0.024 g of $Na_2S_2O_8$ were dissolved in 5 mL $H_2{}^{18}O$ (purchased from Aladdin, 97 atom% ^{18}O) in 10 mL quartz container that was sealed with a rubber septum. Then, 20 mg of the as-obtained CCO/BWO-30% photocatalyst was put into the container, and air was deaerated with He for 60 min. After visible-light illumination for 8 h ($\lambda > 420$ nm), 0.4 mL of the gas product was withdrawn using a gas-tight syringe for gas analysis. A Agilent Technologies 6890 N network GC system combined with a Agilent Technologies 5975B inert XL MSD model mass spectrometer (GC–MS) was used to collect the mass spectrometry data, and the range of *m/z* is from 10 to 50.

3. Results and discussion

3.1. Phase structure

The crystallographic property and phase purity of the as-prepared samples were first examined by the XRD measurements. As shown in Fig. 2, the diffraction peaks of the pure BWO and CCO samples are in good agreement with the orthorhombic phase of Bi_2WO_6 (JCPDS card 39–0256, a = 5.467 Å b = 16.435 Å and c = 5.438 Å) [6] and the orthorhombic phase of $Co(CO_3)_{0.5}(OH)\cdot 0.11H_2O$ (JCPDS card number 48–0083, a = 8.792 Å, b = 10.150 Å and c = 4.433 Å) [34,35]. As for the CCO/BWO composites, all the BWO diffraction peaks were observed, which reveals that the presence of CCO in the reactions did not affect the crystalline structure of BWO. Furthermore, it can be seen that, with the increase of CCO in the CCO/BWO composites, the intensity of diffraction peaks for CCO is gradually enhanced. Diffraction patterns for other impurities were not found in the XRD characterization, confirming high purity of the CCO/BWO nanocomposites.

3.2. Morphology investigation

The morphology and structure of the as-prepared samples were

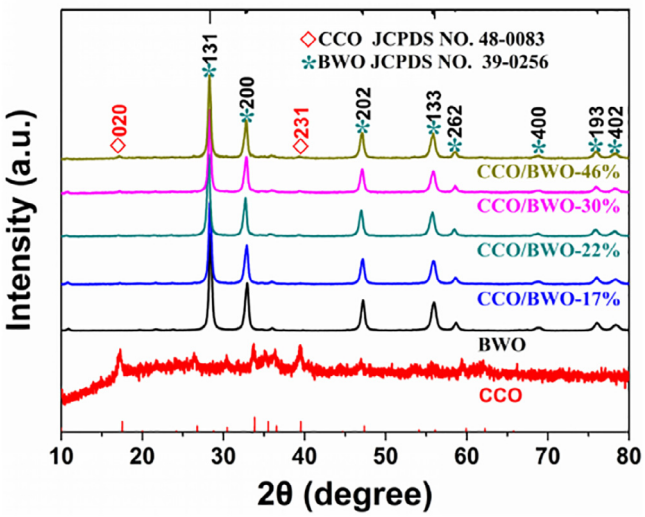

Fig. 2. XRD patterns of the as-prepared different samples.

further characterized by SEM, TEM, and HRTEM. Fig. 3a and b shows the SEM images of pure BWO, which exhibits a sheet-like nanostructure. For comparison, the as-prepared CCO displays a uniform flower-like structure assembled by numerous nanowires, as shown in Fig. S1a, b. The SEM images in Fig. 3c and d of the CCO/BWO-30% composite reveal a hybrid structure of flower-like CCO nanowires decorated with BWO nanosheets. The SEM images of other BWO/CCO composites are provided in Fig. S2, also indicating that the hybrid flower-like nanowires decorated with different amounts of BWO nanosheets depending on the weight ratio. The energy-dispersive X-ray spectrometer (EDS) patterns of the different samples are further presented in Fig. S3, and the atom percentages of Co and Bi elements in the different samples (inset in Fig. S3) can be fitted well with the input of reagents. Additionally, the energy dispersive X-ray (EDX) elemental mapping suggests the uniform distribution of Bi, W, O, Co and C elements in the CCO/BWO hybrid sample (Fig. S4). The TEM image of the CCO/BWO-30% sample in Fig. 3e reveals a hybrid structure as well, which is in a good agreement with the SEM observation. The HRTEM image Fig. 3f recorded from the edge section of CCO/BWO-30% sample, exhibits interplanar spacings of about 0.315 and 0.370 nm, corresponding to the (1 3 1) and (1 1 1) planes of orthorhombic-structured BWO, respectively.

3.3. Investigation of element valence

XPS characterizations were further conducted to reveal the chemical states and compositions of the as-prepared CCO, BWO and CCO/BWO-30% samples, as shown in Fig. 4. The survey XPS spectra of CCO/BWO-30% product contains Bi, Co, W, O and C elements reveal that CCO and BWO are formed composite perfectly (Fig. 4a). Based on the high-resolution Bi 4f spectrum of the BWO sample (Fig. 4b), the peaks at 164.7 and 159.4 eV can be ascribed to the levels of Bi $4f_{5/2}$ and Bi $4f_{7/2}$ spin–orbit splitting photoelectrons in the Bi^{3+} chemical state, respectively [36]. From the W 4f spectra (Fig. 4c), the two bands at 37.8 and 35.6 eV are ascribed to W $4f_{5/2}$ and W $4f_{7/2}$, respectively [6]. The high-resolution XPS spectra of Co 2p (Fig. 4d) exhibit two spin-obit doublets corresponding to the shakeup satellites (identified as “Sat.”). And the two bands at 797.2 and 781.1 eV are attributed to Co $2p_{1/2}$ and Co $2p_{3/2}$ of Co^{3+}, respectively [37,38]. Compared with the pure BWO and CCO samples, the binding energies of the CCO/BWO-30% sample of the Bi 4f and W 4f show a negative shift and Co 2p have a positive shift, indicating that CCO/BWO composite can be successfully synthesized and electrons transfer from the surface of CCO to the surface of BWO [39,40].

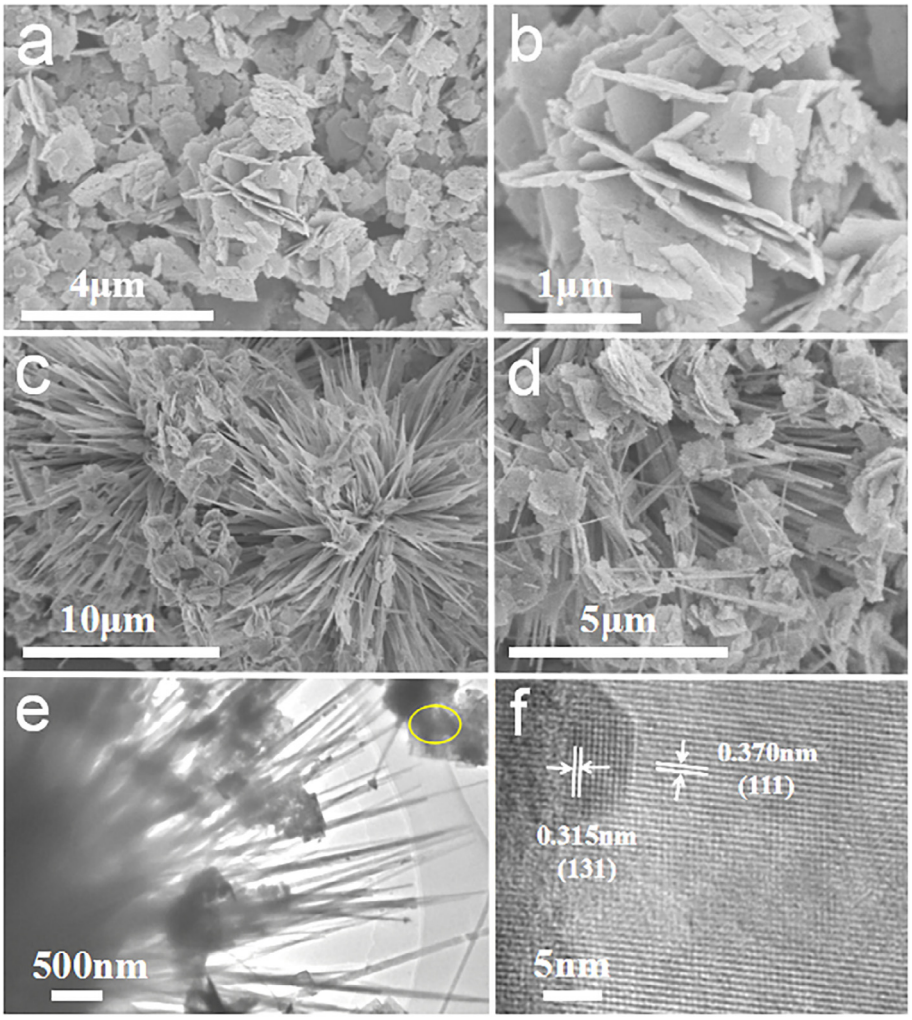

Fig. 3. (a, b) SEM images of the as-prepared BWO nanosheets; (c, d) SEM, (e) TEM, and (f) HRTEM images of the as-prepared CCO/BWO-30% sample.

3.4. Band structures investigation

The optical absorption properties of the as-prepared BWO and CCO samples were investigated by the UV–vis DRS [41,42]. As shown in Fig. 5, the BWO sample shows an absorption edge at around 460 nm which accounts for the visible light photocatalytic activity. The as-prepared CCO sample exhibits two distinct absorption features, the band-edge absorption in the short-wavelength region below 300 nm plus the broad band in the visible region centered at about 500 nm which is due to d-d transitions of Co^{2+} ions in an octahedral geometry [43,44]. The optical band gap of the as-prepared BWO and CCO samples were determined according to the Tauc equation (2) [45]:

$$\alpha h\nu = A(h\nu - E_g)^{n/2} \quad (2)$$

where A, h, v, α, and Eg are a constant, the Planck constant, light frequency, absorption coefficient, and band gap energy, respectively, and n is determined by the optical transition type of the semiconductor, which equals 1 for direct allowed transition and 4 for indirect forbidden transition. The Tauc plots of the as-prepared bare BWO and CCO samples are shown in the inset of Fig. 5a and b, which reveal the corresponding band gap energies of about 2.96 eV and 2.95 eV, respectively. Generally, the flat-band potentials (V_{fb}) of the samples were measured using Mott-Schottky plots. The positive slop of the Mott-Schottky plots for the BWO and CCO samples indicated the n-type nature [46]. And the V_{fb} is located just below the bottom of conduction band (CB) for an n-type semiconductor [47]. As shown in Fig. 6, the value of V_{fb}, as the x intercept of the linear region, is determined to be 0.05 and −1.02 V *vs.* Hg/Hg_2Cl_2 electrode (equivalent to 0.29 and −0.78 V *vs.* NHE), respectively. According to the Eq. (3) [6,32]

$$E_g = E_{VB} - E_{CB} \quad (3)$$

the VBs of the as-prepared BWO and CCO are obtained as 3.25 and 2.17 eV. The relative valence band (VB) and CB of the BWO and CCO samples calculated based on the Mott-Schottky plots are presented in Table S2. The band structures of BWO and CCO indicate that CCO can be excited by visible light irradiation and the photogenerated electrons flow into the CB of BWO due to the higher energy level of the CCO CB, and the photogenerated holes migrate to the surface of CCO nanowires. The coupled band structure leads to efficient separation of photogenerated electron-hole pairs and therefore improves the photocatalytic activity. Owing to the suitable band level alignment, the performance of water oxidation to oxygen can be significantly enhanced under visible-light irradiation.

3.5. Photocatalytic reactivity investigation

The photocatalytic O_2 production performance of the as-prepared samples was examined under visible-light irradiation ($\lambda > 420$ nm). Fig. 7a depicts the O_2 evolution results for different samples as photocatalysts. Accordingly, the photocatalytic activity is ordered as BWO < CCO < CCO/BWO-46% < CCO/BWO-17% < CCO/BWO-22% < CCO/BWO-30%. As shown in Fig. 7b, the O_2 production of

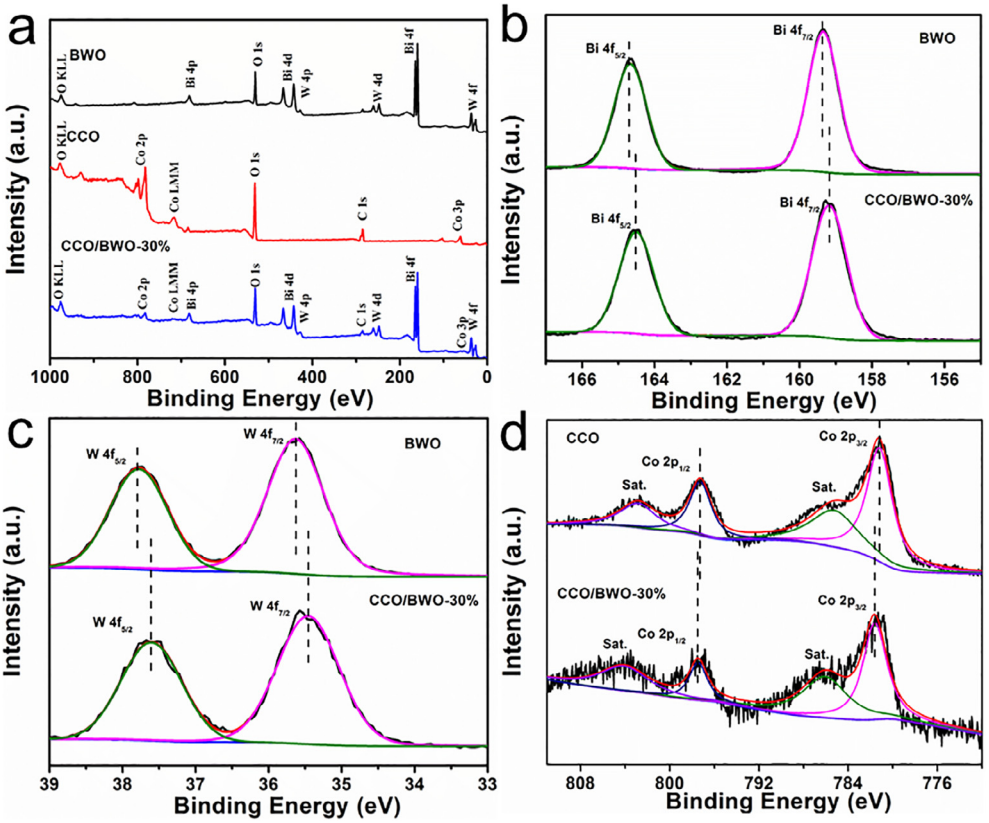

Fig. 4. The XPS spectra of the as-prepared BWO, CCO and CCO/BWO-30% samples: (a) The survey spectra of the different samples, and high-resolution XPS spectra of (b) Bi, (c) W and (d) Co elements.

CCO BWO-30% sample is 953 μmol $h^{-1}g^{-1}$, which is nearly 1.8 and 5.8 times than the CCO and BWO samples, respectively. Considering the alkaline solution is favorable for oxygen evolution, the O_2 evolution performance of the CCO/BWO-30% catalyst at different NaOH concentrations was also measured. As show in Fig. S5, the rate of O_2 evolution is about 623 μmol $g^{-1}h^{-1}$ in neutral solution, a obvious decrease compared with 0.1 M NaOH aqueous solution, whereas the activity has no significant enhancement in 0.5 M NaOH [48,49]. Compared with previously reported BWO-based photocatalysts, the CCO/BWO hybrid obtained in this work possesses the highest photocatalytic O_2 evolution (Table S3). The improved photocatalytic activities of the CCO/BWO hybrid photocatalyst can be attributed to the structural coupling of the BWO nanosheets and CCO nanowires, which accelerates the interfacial separation of photogenerated electron-hole pairs [50,51]. To identify the origin of the detected O_2 produced from water splitting, ^{18}O isotope-labeling experiment was further performed and the $H_2{}^{18}O$ was used as the oxygen source in the photocatalytic process. After irradiation for 8 h, the mass spectrum of GC–MS measurement exhibit that the primary peak is centered at $m/z = 36$ ($^{18}O_2$) (Fig. S6), indicating that O_2 is produced by water decomposition. The apparent quantum yield (AQY) (Fig. 8a) was measured in a way similar to the photocatalytic O_2 production test, utilizing a 300w Xe lamp with 420, 450 and 500 nm band pass filter as the monochromatic light source. For the CCO/BWO-30% sample, the AQY value is 3.19%, 1.82%, and 0.93% at the wavelength of 420, 450 and 500 nm, respectively, which decreases gradually with increased light wavelength. In contrast, the AQY of the as-prepared BWO and CCO samples at 420 nm is measured to be 0.51% and 1.63%, respectively, much lower than that of the hybrid CCO/BWO-30% sample. The above results reveal that the hybrid CCO/BWO photocatalyst containing an appropriate amount of CCO has much higher photocatalytic activity than BWO and CCO. The cyclic test was performed to evaluate the photostability of the CCO, BWO and CCO/

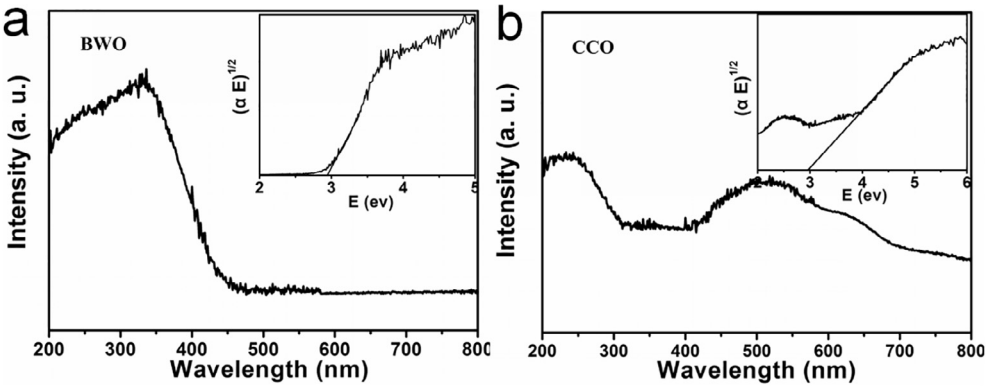

Fig. 5. UV–Vis DRS of the as-prepared (a) BWO and (b) CCO samples and the corresponding Tauc plots (inset).

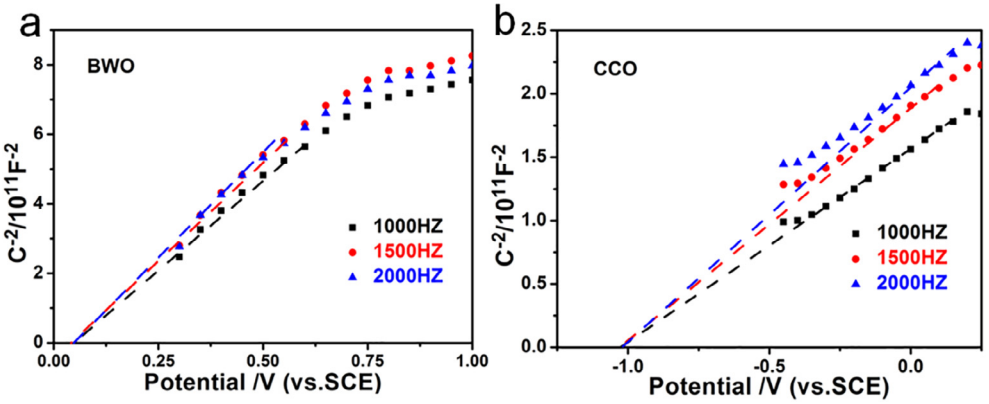

Fig. 6. Mott–Schottky plots of the as-prepared (a) BWO and (b) CCO samples.

BWO-30% photocatalysts (Fig. 8b). In contrast to the CCO and BWO samples, after three consecutive runs of reaction, the CCO/BWO-30% sample exhibits no significant loss of the catalytic activity. Additionally, even under irradiation for 20 h, the as-prepared CCO/BWO-30% sample show no significant decrease, demonstrating the excellent photostability of the product (Fig. S7). After the photocatalytic test, the morphology of CCO/BWO-30% sample has no obvious change compared with the initial samples (Fig. S8a). The XRD patterns (Fig. S8b) of the CCO/BWO-30% photocatalyst before and after cyclic O_2 evolution test also reveal no distinguishable change in the main peaks, indicating much better photostability and durability of the hybrid sample in the photocatalytic O_2 evolution reaction. These results indicate the great potential of CCO/BWO-30% composite as an efficient, stable photocatalyst.

3.6. Photoluminescence spectra and photo-electronic activity

PL spectroscopy is a powerful technique to characterize the recombination behaviors of the photogenerated electron–hole pairs [52]. As shown in Fig. S9, all the samples exhibit a broad emission in the wavelength range of 400–480 nm at a excited wavelength of 300 nm. Compared with the as-prepared bare BWO and other CCO/BWO nanocomposites, the PL response for the CCO/BWO-30% sample exhibits the weakest emission, suggesting greatly reduced radiative recombination of the photogenerated carriers, which can be attributed to the enhanced separation of charge carriers due to formation of the heterojunction between BWO and CCO [53]. It is evidenced that the coupling of BWO with CCO can effectively suppress the recombination of photoinduced charge carriers in BWO and achieve enhanced photocatalytic activity. In order to further characterize charge separation and transfer efficiency in the as-prepared photocatalysts, photocurrent transient response measurements were carried out with multiple 40 s on-off cycles under visible-light irradiation in a three electrode photoelectrochemical cell with 0.1 M Na_2SO_4 solution and an Hg/Hg^{2+} in saturated KCl as the reference electrode and a Pt wire as the counter electrode [6,33,54]. As shown in Fig. 9a, the CCO/BWO-30% sample shows the highest current density, indicating a larger separation rate of the photoinduced electron-hole pairs in the CCO/BWO-30% sample. Fig. 9b shows the EIS Nyquist plots of all the prepared composite photocatalysts, and the CCO/BWO-30% sample presents a smaller circular radius than the others, suggesting larger carrier transfer rate and higher charge separation efficiency [55,56]. With optimal CCO content, the CCO/BWO-30% sample exhibits the lowest resistance and the highest photocurrent, due to the mediation of interfacial charge dynamics [57,58]. Moreover, the extended surface of the CCO nanowires facilitates the transfer of photogenerated electrons.

3.7. Photocatalytic mechanism

Based on our experimental results, the reaction mechanism of the CCO/BWO composites for photocatalytic water oxidation was depicted in Fig. 10. The energy bandgap of BWO is 2.96 eV, and its CB and VB energy levels are located at about 0.29 and 3.25 eV (*vs.* NHE), respectively. The CB and VB energy levels of CCO are at about −0.78 and 2.17 eV (*vs.* NHE), respectively. The CB edge potential of CCO is more negative than that of BWO, while the VB of BWO is more positive than that of CCO. The local electric field at the CCO/BWO interface drives the photogenerated electrons toward the CB of BWO, and holes towards the VB of CCO. Since $Na_2S_2O_8$ was used in this work as the electron-scavenging reagent, photogenerated electrons can be scavenged and holes transfer to CCO for oxygen evolution reaction. The efficient separation of photogenerated electrons and holes can be achieved in the

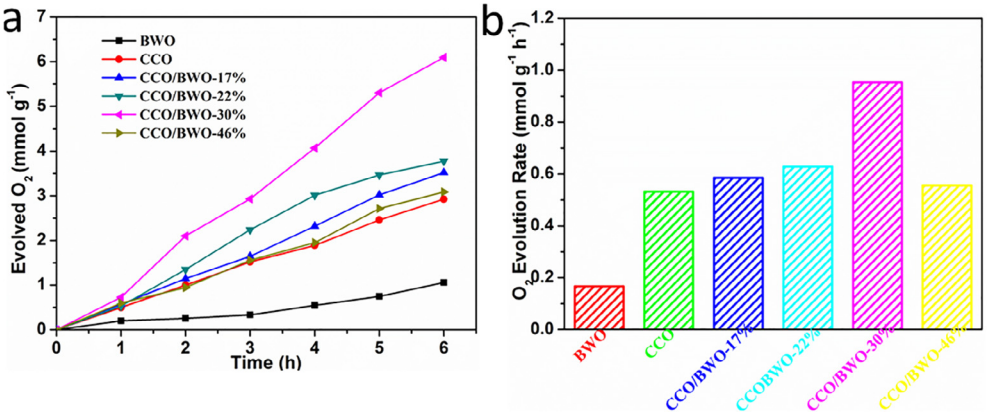

Fig. 7. (a) Time-dependent photocatalytic oxygen evolution and (b) Oxygen evolution rates of the as-prepared samples.

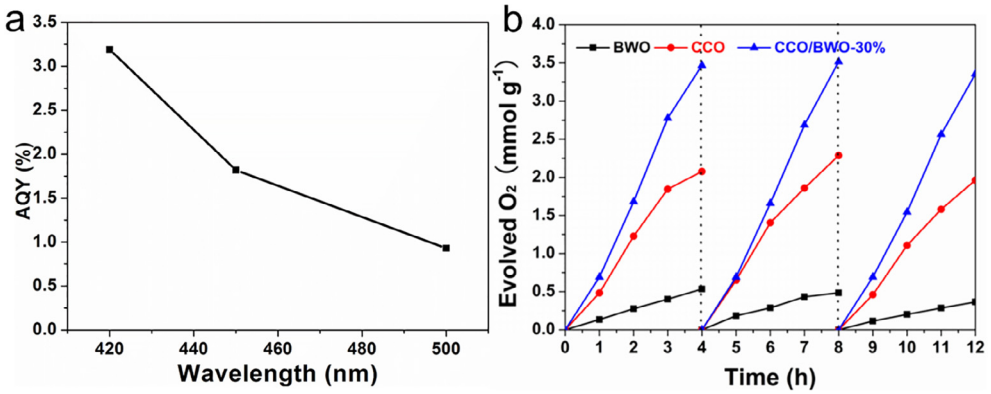

Fig. 8. (a) The apparent quantum yield test of the as-prepared CCO/BWO-30% photocatalyst, (b) cyclic runs for the photocatalytic O_2 evolution using different samples as photocatalysts.

CCO/BWO hybrid photocatalyst, and the enhanced the photocatalytic activity and photostability can be therefore obtained. Additionally, hydroxides can be considered as compounds with great affinity to aqueous medium, which enables strong connection with various semiconductors, and therefore improves the efficiency of photocatalytic oxidation in water oxidation reaction. These features suggest that CCO is an ideal candidate for photocatalytic water splitting. In order to confirm the photo-generated carriers separation process, the active hydroxyl radicals (·OH) were further traced by an ESR spin-trapping technique with DMPO as a spin trap to stabilize radicals under visible-light illumination, using the as-prepared bare BWO, CCO and CCO/BWO-30% samples as catalysts (Fig. S10). From the ESR signal of bare BWO sample, the characteristic peaks of DMPO−•OH adducts are obviously observed. But there are no obvious peaks in the CCO and CCO/BWO-30% photocatalysts, indicating the photo-generated holes migration from BWO to CCO [59,60].

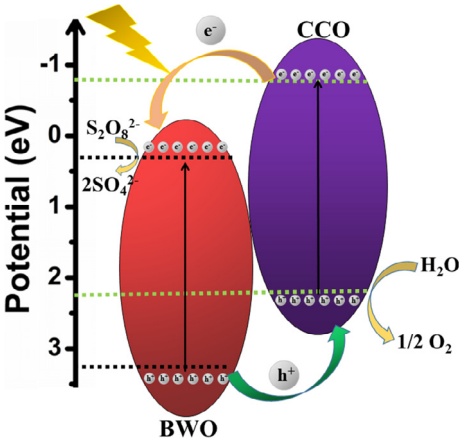

Fig. 10. Schematic illustration for the charge transfer and separation in the CCO/BWO hybrid photocatalyst.

4. Conclusions

In summary, we report a novel CCO/BWO hybrid photocatalyst which was successfully prepared via a facile hydrothermal method. Without utilizing any additional cocatalyst, the as-prepared CCO/BWO composites exhibit enhanced photocatalytic activity and photostability for water oxidation under visible-light irradiation. The composite with optimal CCO content of 30% exhibits the highest O_2 production of 953 μmol h^{-1} g^{-1}, which is nearly 1.8 and 5.8 times that of pure CCO and BWO samples, respectively. It has been experimentally revealed that the photogenerated electrons move to the surface of BWO and the holes to the surface of CCO, which significantly reduces the probability of electron-hole recombination and increases the efficiency of carrier separation. This work will provide a new insight into the construction of cocatalyst-free visible-light-driven hybrid composites for photocatalytic water oxidation and energy conversion applications.

Conflicts of interest

There are no conflicts to declare.

Acknowledgments

Y. Hu acknowledges the financial support from Natural Science Foundation of China (21671173). J. Q. Ning acknowledges the financial support from Natural Science Foundation of China (11874390) and Hundred Talents Program of Chinese Academy of Sciences.

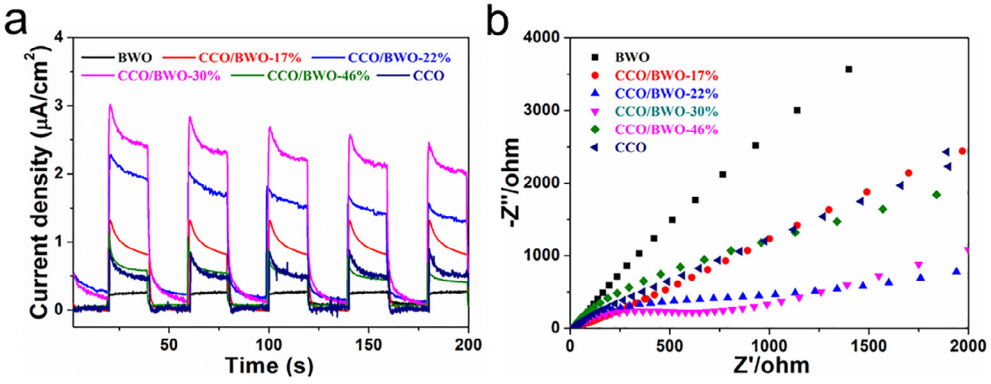

Fig. 9. (a) Photocurrent responses of the different samples under visible-light illumination, (b) EIS Nyquist plots of the different samples.

Appendix A. Supplementary data

Supplementary data to this article can be found online at https://doi.org/10.1016/j.cej.2018.11.094.

References:

[1] J. Liu, J. Diamond, China's environment in a globalizing world, Nature 435 (2005) 1179–1186.
[2] N. Armaroli, V. Balzani, The future of energy supply: challenges and opportunities, Angew. Chem. Int. Ed. 46 (2007) 52–66.
[3] K. Kaygusuz, Energy and environmental issues relating to greenhouse gas emissions for sustainable development in Turkey, Renewable Sustainable Energy Rev. 13 (2009) 253–270.
[4] S.E. Hosseini, M.A. Wahid, Hydrogen production from renewable and sustainable energy resources: Promising green energy carrier for clean development, Renewable Sustainable Energy Rev. 57 (2016) 850–866.
[5] L. Wang, Y. Wan, Y. Ding, Y. Niu, Y. Xiong, X. Wu, H. Xu, Photocatalytic oxygen evolution from low-bandgap conjugated microporous polymer nanosheets: a combined first-principles calculation and experimental study, Nanoscale 9 (2017) 4090–4096.
[6] A. Etogo, R. Liu, J.B. Ren, L.W. Qi, C.C. Zheng, J.Q. Ning, Y.J. Zhong, Y. Hu, Facile one-pot solvothermal preparation of Mo doped Bi_2WO_6 biscuit-like microstructures for visible-light-driven photocatalytic water oxidation, J. Mater. Chem. A 4 (2016) 13242–13250.
[7] J. Luo, J.-H. Im, M.T. Mayer, M. Schreier, M.K. Nazeeruddin, N.-G. Park, S.D. Tilley, H.J. Fan, M. Graetzel, Water photolysis at 12.3% efficiency via perovskite photovoltaics and Earth-abundant catalysts, Science 345 (2014) 1593–1596.
[8] Y. Liang, Y. Li, H. Wang, J. Zhou, J. Wang, T. Regier, H. Dai, Co_3O_4 nanocrystals on graphene as a synergistic catalyst for oxygen reduction reaction, Nat. Mater. 10 (2011) 780.
[9] J. Rosen, G.S. Hutchings, F. Jiao, Ordered mesoporous cobalt oxide as highly efficient oxygen evolution catalyst, J. Am. Chem. Soc. 135 (2013) 4516–4521.
[10] C.-C. Lin, Y. Guo, J. Vela, Microstructure effects on the water oxidation activity of Co_3O_4/porous silica nanocomposites, ACS Catal. 5 (2015) 1037–1044.
[11] L. Cao, F. Xu, Y.-Y. Liang, H.-L. Li, Preparation of the novel nanocomposite Co $(OH)_2$/ ultra-stable y zeolite and its application as a supercapacitor with high energy density, Adv. Mater. 16 (2004) 1853–1857.
[12] R. Ma, K. Takada, K. Fukuda, N. Iyi, Y. Bando, T. Sasaki, Topochemical synthesis of monometallic (Co^{2+}–Co^{3+}) layered double hydroxide and its exfoliation into positively charged $Co(OH)_2$ nanosheets, Angew. Chem. Int. Ed. 47 (2008) 86–89.
[13] Y. Liu, H. Cheng, M. Lyu, S. Fan, Q. Liu, W. Zhang, Y. Zhi, C. Wang, C. Xiao, S. Wei, B. Ye, Y. Xie, Low overpotential in vacancy-rich ultrathin $CoSe_2$ nanosheets for water oxidation, J. Am. Chem. Soc. 136 (2014) 15670–15675.
[14] M. Barroso, A.J. Cowan, S.R. Pendlebury, M. Grätzel, D.R. Klug, J.R. Durrant, The role of cobalt phosphate in enhancing the photocatalytic activity of α-Fe_2O_3 toward water oxidation, J. Am. Chem. Soc. 133 (2011) 14868–14871.
[15] Y. Wang, Y. Wang, R. Jiang, R. Xu, Cobalt phosphate–ZnO composite photocatalysts for oxygen evolution from photocatalytic water oxidation, Ind. Eng. Chem. Res. 51 (2012) 9945–9951.
[16] H. Chen, D. Jiang, Z. Sun, R.M. Irfan, L. Zhang, P. Du, Cobalt nitride as an efficient cocatalyst on CdS nanorods for enhanced photocatalytic hydrogen production in water, Catal. Sci. Technol. 7 (2017) 1515–1522.
[17] S. Zhu, Z. Wang, F. Huang, H. Zhang, S. Li, Hierarchical $Cu(OH)_2$@$Ni_2(OH)_2CO_3$ core/shell nanowire arrays in situ grown on three-dimensional copper foam for high-performance solid-state supercapacitors, J. Mater. Chem. A 5 (2017) 9960–9969.
[18] W. Wei, S. Cui, L. Ding, L. Mi, W. Chen, X. Hu, Urchin-like $Ni_{1/3}Co_{2/3}(CO_3)_{1/2}(OH)\cdot 0.11H_2O$ for ultrahigh-rate electrochemical supercapacitors: structural evolution from solid to hollow, ACS Appl. Mater. Interfaces 9 (2017) 40655–40670.
[19] Y. Zhang, Q. Xiao, X. Guo, X. Zhang, Y. Xue, L. Jing, X. Zhai, Y.-M. Yan, K. Sun, A novel electrocatalyst for oxygen evolution reaction based on rational anchoring of cobalt carbonate hydroxide hydrate on multiwall carbon nanotubes, J. Power Sources 278 (2015) 464–472.
[20] Y. Wang, W. Ding, S. Chen, Y. Nie, K. Xiong, Z. Wei, Cobalt carbonate hydroxide/C: an efficient dual electrocatalyst for oxygen reduction/evolution reactions, Chem. Commun. 50 (2014) 15529–15532.
[21] W. Wang, M. Ma, M. Kong, Y. Yao, N. Wei, Cobalt carbonate hydroxide hydrate nanowires array: a three-dimensional catalyst electrode for effective water oxidation, Micro. Nano. Lett. 12 (2017) 264–266.
[22] N. Zhang, R. Ciriminna, M. Pagliaro, Y.-J. Xu, Nanochemistry-derived Bi_2WO_6 nanostructures: towards production of sustainable chemicals and fuels induced by visible light, Chem. Soc. Rev. 43 (2014) 5276–5287.
[23] H. Huang, R. Cao, S. Yu, K. Xu, W. Hao, Y. Wang, F. Dong, T. Zhang, Y. Zhang, Single-unit-cell layer established Bi_2WO_6 3D hierarchical architectures: efficient adsorption, photocatalysis and dye-sensitized photoelectrochemical performance, Appl. Catal., B 219 (2017) 526–537.
[24] P. Ju, P. Wang, B. Li, H. Fan, S. Ai, D. Zhang, Y. Wang, A novel calcined Bi_2WO_6/$BiVO_4$ heterojunction photocatalyst with highly enhanced photocatalytic activity, Chem. Eng. J. 236 (2014) 430–437.
[25] H. Huang, X. Han, X. Li, S. Wang, P.K. Chu, Y. Zhang, Fabrication of multiple heterojunctions with tunable visible-light-active photocatalytic reactivity in BiOBr–BiOI full-range composites based on microstructure modulation and band structures, ACS Appl. Mater. Interfaces 7 (2015) 482–492.
[26] M.-S. Gui, W.-D. Zhang, Y.-Q. Chang, Y.-X. Yu, One-step hydrothermal preparation strategy for nanostructured WO_3/Bi_2WO_6 heterojunction with high visible light photocatalytic activity, Chem. Eng. J. 197 (2012) 283–288.
[27] Y. Wang, X. Bai, C. Pan, J. He, Y. Zhu, Enhancement of photocatalytic activity of Bi_2WO_6 hybridized with graphite-like C_3N_4, J. Mater. Chem. 22 (2012) 11568–11573.
[28] Y. Zhu, Y. Wang, Q. Ling, Y. Zhu, Enhancement of full-spectrum photocatalytic activity over $BiPO_4$/Bi_2WO_6 composites, Appl. Catal., B 200 (2017) 222–229.
[29] L. Zhang, K.-H. Wong, Z. Chen, J.C. Yu, J. Zhao, C. Hu, C.-Y. Chan, P.-K. Wong, AgBr/Ag/ Bi_2WO_6 nanojunction system: a novel and efficient photocatalyst with double visible-light active components, Appl. Catal., A 363 (2009) 221–229.
[30] J. Yang, D. Wang, H. Han, C. Li, Roles of cocatalysts in photocatalysis and photoelectrocatalysis, Acc. Chem. Res. 46 (2013) 1900–1909.
[31] F. Wang, Y. Jiang, D.J. Lawes, G.E. Ball, C. Zhou, Z. Liu, R. Amal, Analysis of the promoted activity and molecular mechanism of hydrogen production over fine Au–Pt alloyed TiO_2 photocatalysts, ACS Catal. 5 (2015) 3924–3931.
[32] R. Liu, J.B. Ren, D. Zhao, J.Q. Ning, Z.Y. Zhang, Y.J. Wang, Y.J. Zhong, C.C. Zheng, Y. Hu, Band-gap engineering of porous $BiVO_4$ nanoshuttles by Fe and Mo co-doping for efficient photocatalytic water oxidation, Inorg Chem. Front. 4 (2017) 2045–2054.
[33] B. He, R. Liu, J. Ren, C. Tang, Y. Zhong, Y. Hu, One-step solvothermal synthesis of petalous carbon-coated Cu^+-doped CdS nanocomposites with enhanced photocatalytic hydrogen production, Langmuir 33 (2017) 6719–6726.
[34] B. Wang, T. Zhu, H.B. Wu, R. Xu, J.S. Chen, X.W. Lou, Porous Co_3O_4 nanowires derived from long $Co(CO_3)_{0.5}(OH)\cdot 0.11H_2O$ nanowires with improved supercapacitive properties, Nanoscale 4 (2012) 2145–2149.
[35] S. Xiong, J.S. Chen, X.W. Lou, H.C. Zeng, Mesoporous Co_3O_4 and CoO@C topotactically transformed from chrysanthemum-like $Co(CO_3)_{0.5}(OH)\cdot 0.11H_2O$ and their lithium-storage properties, Adv. Funct. Mater. 22 (2012) 861–871.
[36] H. Huang, K. Xiao, T. Zhang, F. Dong, Y. Zhang, Rational design on 3D hierarchical bismuth oxyiodides via in situ self-template phase transformation and phase-junction construction for optimizing photocatalysis against diverse contaminants, Appl. Catal., B 203 (2017) 879–888.
[37] E.L. Hu, Y.F. Feng, J.W. Nai, D. Zhao, Y. Hu, X.W. Lou, Construction of hierarchical Ni-Co-P hollow nanobricks with oriented nanosheets for efficient overall water splitting, Energy Environ. Sci. 11 (2018) 872–880.
[38] E. Hu, J. Ning, D. Zhao, C. Xu, Y. Lin, Y. Zhong, Z. Zhang, Y. Wang, Y. Hu, A room-temperature postsynthetic ligand exchange strategy to construct mesoporous Fe-doped CoP hollow triangle plate arrays for efficient electrocatalytic water splitting, Small 14 (2018) e1704233.
[39] L. Ye, J. Liu, C. Gong, L. Tian, T. Peng, L. Zan, Two different roles of metallic Ag on Ag/AgX/BiOX (X = Cl, Br) visible light photocatalysts: surface plasmon resonance and Z-Scheme bridge, ACS Catal. 2 (2012) 1677–1683.
[40] S. Dong, X. Ding, T. Guo, X. Yue, X. Han, J. Sun, Self-assembled hollow sphere shaped Bi_2WO_6/RGO composites for efficient sunlight-driven photocatalytic degradation of organic pollutants, Chem. Eng. J. 316 (2017) 778–789.
[41] X. Gao, H.B. Wu, L. Zheng, Y. Zhong, Y. Hu, X.W. Lou, Formation of mesoporous heterostructured $BiVO_4$/Bi_2S_3 hollow discoids with enhanced photoactivity, Angew. Chem. Int. Ed. 53 (2014) 5917–5921.
[42] W. Yang, L. Zhang, Y. Hu, Y. Zhong, H.B. Wu, X.W. Lou, Microwave-assisted synthesis of porous Ag_2S-Ag hybrid nanotubes with high visible-light photocatalytic activity, Angew. Chem. Int. Ed. 51 (2012) 11501–11504.
[43] X. Guo, L. Wang, S. Yue, D. Wang, Y. Lu, Y. Song, J. He, Single-crystalline organic–inorganic layered cobalt hydroxide nanofibers: facile synthesis, characterization, and reversible water-induced structural conversion, Inorg. Chem. 53 (2014) 12841–12847.
[44] X. Yang, Y. Zhang, F. Li, T. Guo, Y. Wu, F. Jin, M. Fang, Y. Lan, Y. Li, Y. Zhou, Z. Zou, Theoretical and experimental studies on three water-stable, isostructural, paddlewheel based semiconducting metal–organic frameworks, Dalton Trans. 46 (2017) 8204–8218.
[45] J. Tauc, R. Grigorovici, A. Vancu, Optical properties and electronic structure of amorphous germanium, Phys. status solidi B 15 (1966) 627–637.
[46] J. Boltersdorf, I. Sullivan, T.L. Shelton, Z. Wu, M. Gray, B. Zoellner, F.E. Osterloh, P.A. Maggard, Flux synthesis, optical and photocatalytic properties of n-type sn2tio4: hydrogen and oxygen evolution under visible light, Chem. Mater. 28 (2016) 8876–8889.
[47] S.J. Hong, S. Lee, J.S. Jang, J.S. Lee, Heterojunction $BiVO_4$/WO_3 electrodes for enhanced photoactivity of water oxidation, Energy Environ. Sci. 4 (2011) 1781–1787.
[48] M. Murakami, D. Hong, T. Suenobu, S. Yamaguchi, T. Ogura, S. Fukuzumi, Catalytic mechanism of water oxidation with single-site ruthenium–heteropolytungstate complexes, J. Am. Chem. Soc. 133 (2011) 11605–11613.
[49] D.J. Wasylenko, C. Ganesamoorthy, M.A. Henderson, B.D. Koivisto, H.D. Osthoff, C.P. Berlinguette, Electronic modification of the $[RuII(tpy)(bpy)(OH_2)]^{2+}$ scaffold: effects on catalytic water oxidation, J. Am. Chem. Soc. 132 (2010) 16094–16106.
[50] H. Huang, Y. He, X. Du, P.K. Chu, Y. Zhang, A general and facile approach to heterostructured Core/Shell $BiVO_4$/BiOI p–n junction: room-temperature in situ assembly and highly boosted visible-light photocatalysis, ACS Sustain. Chem. Eng. 3 (2015) 3262–3273.
[51] H. Huang, K. Xiao, Y. He, T. Zhang, F. Dong, X. Du, Y. Zhang, In situ assembly of BiOI@Bi12O17Cl 2 p-n junction: charge induced unique front-lateral surfaces coupling heterostructure with high exposure of BiOI 001 active facets for robust and nonselective photocatalysis, Appl. Catal., B 199 (2016) 75–86.
[52] Y. Hu, X. Gao, L. Yu, Y. Wang, J. Ning, S. Xu, X.W. Lou, Carbon-coated CdS petalous nanostructures with enhanced photostability and photocatalytic activity, Angew. Chem. Int. Ed. 52 (2013) 5636–5639.

[53] S.J.A. Moniz, S.A. Shevlin, D.J. Martin, Z.-X. Guo, J. Tang, Visible-light driven heterojunction photocatalysts for water splitting – a critical review, Energy Environ. Sci. 8 (2015) 731–759.
[54] J. Ren, D. Zhao, H. Liu, Y. Zhong, J. Ning, Z. Zhang, C. Zheng, Y. Hu, Electrospinning preparation of Sn^{4+}-doped $BiFeO_3$ nanofibers as efficient visible-light-driven photocatalyst for O_2 evolution, J. Alloys Compd. 766 (2018) 274–283.
[55] B. He, Z. Li, D. Zhao, H. Liu, Y. Zhong, J. Ning, Z. Zhang, Y. Wang, Y. Hu, Fabrication of porous Cu-doped $BiVO_4$ nanotubes as efficient oxygen-evolving photocatalysts, ACS Appl. Nano Mater. 1 (2018) 2589–2599.
[56] K. Li, M. Han, R. Chen, S.-L. Li, S.-L. Xie, C. Mao, X. Bu, X.-L. Cao, L.-Z. Dong, P. Feng, Y.-Q. Lan, Hexagonal@cubic CdS core@shell nanorod photocatalyst for highly active production of H_2 with unprecedented stability, Adv. Mater. 28 (2016) 8906–8911.
[57] L. Troian-Gautier, B.N. DiMarco, R.N. Sampaio, S.L. Marquard, G.J. Meyer, Evidence that ΔS‡ controls interfacial electron transfer dynamics from anatase TiO_2 to molecular acceptors, J. Am. Chem. Soc. 140 (2018) 3019–3029.
[58] G. Zhang, B. Lin, Y. Qiu, L. He, Y. Chen, B. Gao, Highly efficient visible-light-driven photocatalytic hydrogen generation by immobilizing CdSe nanocrystals on ZnCr-layered double hydroxide nanosheets, Int. J. Hydrogen Energy 40 (2015) 4758–4765.
[59] X. She, J. Wu, H. Xu, J. Zhong, Y. Wang, Y. Song, K. Nie, Y. Liu, Y. Yang, M.F. Rodrigues, R. Vajtai, J. Lou, D. Du, H. Li, P.M. Ajayan, High effciency photocatalytic water splitting using 2D α-Fe_2O_3/g-C_3N_4 Z-scheme catalysts, Adv. Energy Mater. 7 (2017) 1700025.
[60] R. Ye, H. Fang, Y. Zheng, N. Li, Y. Wang, X. Tao, Fabrication of $CoTiO_3$/g-C_3N_4 hybrid photocatalysts with enhanced H_2 evolution: Z-scheme photocatalytic mechanism insight, ACS Appl. Mater. Interfaces 8 (2016) 13879–13889.